nature communications

Article

https://doi.org/10.1038/s41467-026-68381-9

Host-guest strategy for full-visible-spectrum piezochromism in halogen-bonded organic frameworks

Received: 30 June 2025

Accepted: 5 January 2026

Published online: 13 January 2026

Check for updates

Binhao Yang[1], Yixuan Wang[1] ✉, Jiaju Liang[1], Kaiyan Yuan[1], Ruidong Qiao[1], Tao Zhang[2] ✉, Xinyi Yang[1] ✉ & Bo Zou[1,3] ✉

Full-visible-spectrum piezochromism is vital for advanced anti-counterfeiting and storage device applications, yet remains challenging. Polycyclic aromatic hydrocarbons represent a promising class of piezochromic materials. However, pressure-induced structural disorder severely limits their performance by causing photoluminescence (PL) quenching through energy dissipation. In framework materials, host-guest modes offer a promising avenue to overcome the limitations. Herein, we demonstrate that the halogen-bonded organic framework host incorporating acridine guests (denoted as XOF@AD) enables full-visible-spectrum piezochromism modulation with the PL red-shift of 237 nm during compression. Both experiments and calculations reveal that strengthened π−hole···π interactions lower its interaction energy to preserve the structural rigidity of XOF host. This suppresses the structural disorder of AD guests and maintains their enhanced π−π stacking interactions, which leads to a decreased band gap. This work establishes host-guest 3D-XOF as a superior platform that achieves full-visible-spectrum piezochromism and presents promising potential for pressure-responsive sensing.

Full-visible-spectrum piezochromic materials have aroused considerable attention in the field of anti-counterfeiting, storage devices and intelligent responsive, because of its tunable molecular stacking structures under high pressure[1–6]. Purely organic polycyclic aromatic hydrocarbons (PAHs) emerged as promising candidates for full-visible-spectrum piezochromic materials due to their intrinsic π−π stacking arrangement[7,8]. However, most PAHs are prone to undergo pressure-induced amorphization. It is challenging to observe their full-visible-spectrum emission behavior as this disordered structure results in a loose molecular packing mode, which subsequently quenches the photoluminescence (PL) through energy dissipation caused by vibration[9–12]. Tremendous advances have been made to achieve a wide range of tunable PL wavelengths by constructing a rigid environment through designing crystalline porous materials (CPMs) based on PAHs[13–15]. Yet, the piezochromic performance of most CPMs are severely hampered owing to the low crystallinity and inferior structural reversibility. In light of this, how to implement full-visible-spectrum piezochromism accompanied by PL wavelength shifts exceeding 190 nm within the visible range has been the main focus in piezochromic materials.

To tackle the aforementioned limitation, taking advantage of host-guest strategy to encapsulate guest in CPMs can maintain the structural integrity of guest molecules, holding the promise of achieving full-visible-spectrum piezochromic behavior[16–18]. Among them, three-dimensional halogen-bonded organic frameworks (3D-XOFs) constitute a compelling category of CPMs, characterized by directional halogen bonds as structural nodes and high crystallinity[19–21]. These 3D-XOFs establish unique platforms for the

[1]State Key Laboratory of High Pressure and Superhard Materials, Synergetic Extreme Condition High-Pressure Science Center, College of Physics, Jilin University, Changchun, China. [2]Department of Gastrointestinal Colorectal and Anal Surgery, China-Japan Union Hospital of Jilin University, Changchun, China. [3]Department of Physics, College of Science, Yanbian University, Yanji, China. ✉e-mail: wangyixuan19@jlu.edu.cn; taozhang@jlu.edu.cn; yangxinyi@jlu.edu.cn; zoubo@jlu.edu.cn

host-guest strategy by providing nanopores to encapsulate PAH guests. Due to the synergistic combination of π−hole···π interactions and robust halogen bonds, 3D-XOF is endowed with exceptional structural rigidity to resist collapse. This enables the preservation of PAH molecular alignment under high pressure and effectively suppressing amorphization (Fig. 1). Furthermore, 3D-XOFs serve as exceptional hosts that facilitate the formation of parallel-offset π−π stacking configuration in PAH guests to drive their optimal and considerable piezochromic behavior. Therefore, this class of 3D-XOF@PAH (3D-XOF host combined with PAH guests) has emerged as a highly promising candidate for light-emitting materials owing to its superior optoelectronic properties and pressure responsiveness[22–25]. Given that the PL emission variations are predominantly influenced by pressure-induced reductions in intermolecular distances and enhanced molecular interactions, the utilization of 3D-XOF@PAH presents an effective strategy to realize full-visible-spectrum piezochromism[26,27].

Herein, we demonstrate that the host-guest XOF@AD (3D-XOF host combined with acridine guests) achieves full-visible-spectrum piezochromic behavior, accompanied by a PL emission red-shift of 237 nm under hydrostatic compression. This considerable PL emission tunability spans from deep blue (2.81 eV) to red (1.83 eV), exceeding the performance of all previously reported visible-range piezochromic materials. Studies on the mechanisms of pressure-induced structural evolution have elucidated that intensified π−hole···π interactions rigidify the 3D-XOF host by lowering the interaction energy under high pressure. This structural reinforcement effectively inhibits the amorphous phase transition in AD guests while maintaining their enhanced π−π stacking arrangement, which serves as the critical factor enabling full-visible-spectrum piezochromism. In addition, pressure-induced emission enhancement (PIEE) behavior was observed at a mild pressure of 1.2 GPa, attributed to the restriction of chemical bond vibrations-mediated suppression of non-radiative decay pathways.

Results

Crystal structure and PL properties of XOF@AD

The synthesis of XOF@AD was modified from co-crystal engineering method according to the literature[28]. At ambient conditions, 3D-XOF host provides rigid hexagonal-channels to accommodate AD guest molecules, thereby forming the XOF@AD assembly. Adjacent AD molecules are stabilized by intermolecular parallel-offset π−π stacking, while the host-guest assembly is further reinforced by weak C−H···C/F hydrogen bonds (Fig. 2a and Supplementary Fig. 1). Due to π−hole···π interactions between alternately reversed 4-phenylpyridine-N-oxide (PPNO) molecules from adjacent chains, the channel units propagate infinitely along the *c*-axis to generate the 3D-XOF. The non-coplanar conformation of PPNO molecules within the 3D-XOF directly induces self-quenching in the extended network. As a consequence, XOF@AD exhibits a deep blue emission centered at 442 nm under 355 nm excitation, which predominantly originates from the PL of the encapsulated AD guests at ambient conditions (Supplementary Fig. 2). Then, we loaded XOF@AD samples with a culet size of 400 μm and 150 μm diameter cavity in a symmetric diamond anvil cell (DAC) to pressurize. The normalized PL spectrum of XOF@AD displays a remarkable and considerable red-shift up to 237 nm from 1 atm to 22.8 GPa (Fig. 2b and Supplementary Fig. 3). This shift corresponds to a chromatic transition from deep blue (2.81 eV) to red (1.83 eV), spanning nearly the entire visible range. A series of optical photomicrographs unambiguously demonstrated the progressive color evolution (Fig. 2c). Complementing these observations, the pressure-dependent shift in Commission Internationale de l'Éclairage (CIE) coordinates from (0.16, 0.12) at 1 atm to (0.51, 0.34) at 22.8 GPa confirms the polychromatic variation of the PL emission (Fig. 2d). As shown in Fig. 2e, the pressure-dependent wavelength of XOF@AD exhibits a nearly linear correlation with applied pressure ($R^2 = 0.99$) with a sensitivity of 9.82 nm·GPa^{-1}. This high linearity enables precise mapping of the wide color gamut to specific pressures and demonstrates the potential pressure-sensing applications of XOF@AD. Furthermore, the pronounced piezochromic behavior retains robustness over ten consecutive pressure-release cycles, thereby confirming that the optical reversibility of XOF@AD remains largely preserved under extreme conditions (Supplementary Figs. 4, 5). The first compression cycle exhibits a gradual PIEE that reaches the maximum intensity at 1.2 GPa before progressively attenuating at higher pressures (Fig. 2f). This is the first report of PIEE in host-guest 3D-XOF systems. To quantitatively assess the pressure-dependent PL enhancement, the PL quantum yield (PLQY) was evaluated using a previously established protocol, which increases from 10.8% at 1 atm to 22.3% at 1.2 GPa (Supplementary Fig. 6)[29,30]. To further validate the PIEE phenomenon under 1.2 GPa, we performed time-

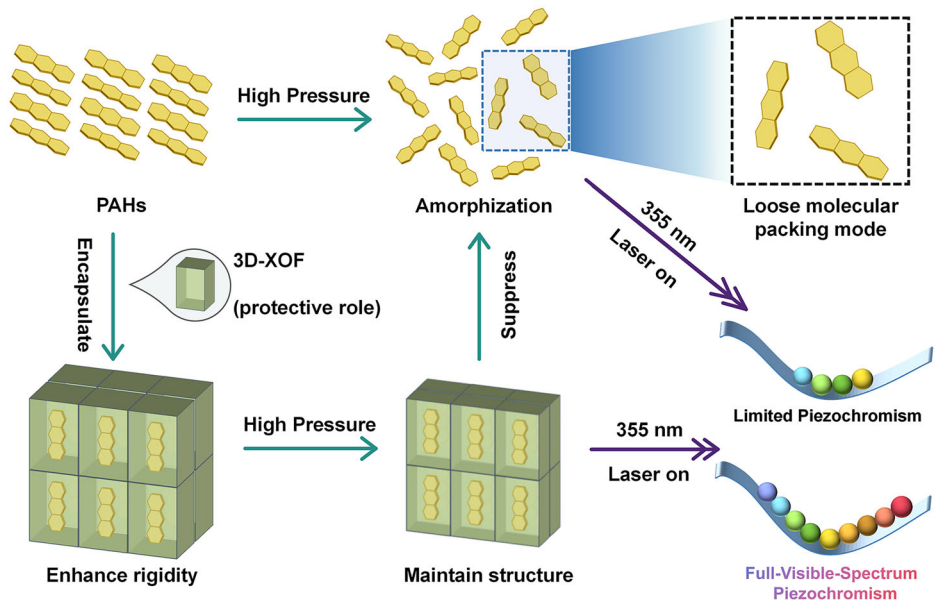

Fig. 1 | Schematic illustration of host-guest strategy for achieving full-visible-spectrum piezochromism. The pressure-induced amorphization severely limits the piezochromic performance of PAHs due to the loose molecular packing mode. 3D-XOF serves a protective role in PAH encapsulation, which suppresses guest amorphization under high pressure to improve the piezochromic performance. The multicolored balls represent the piezochromic capability of the material.

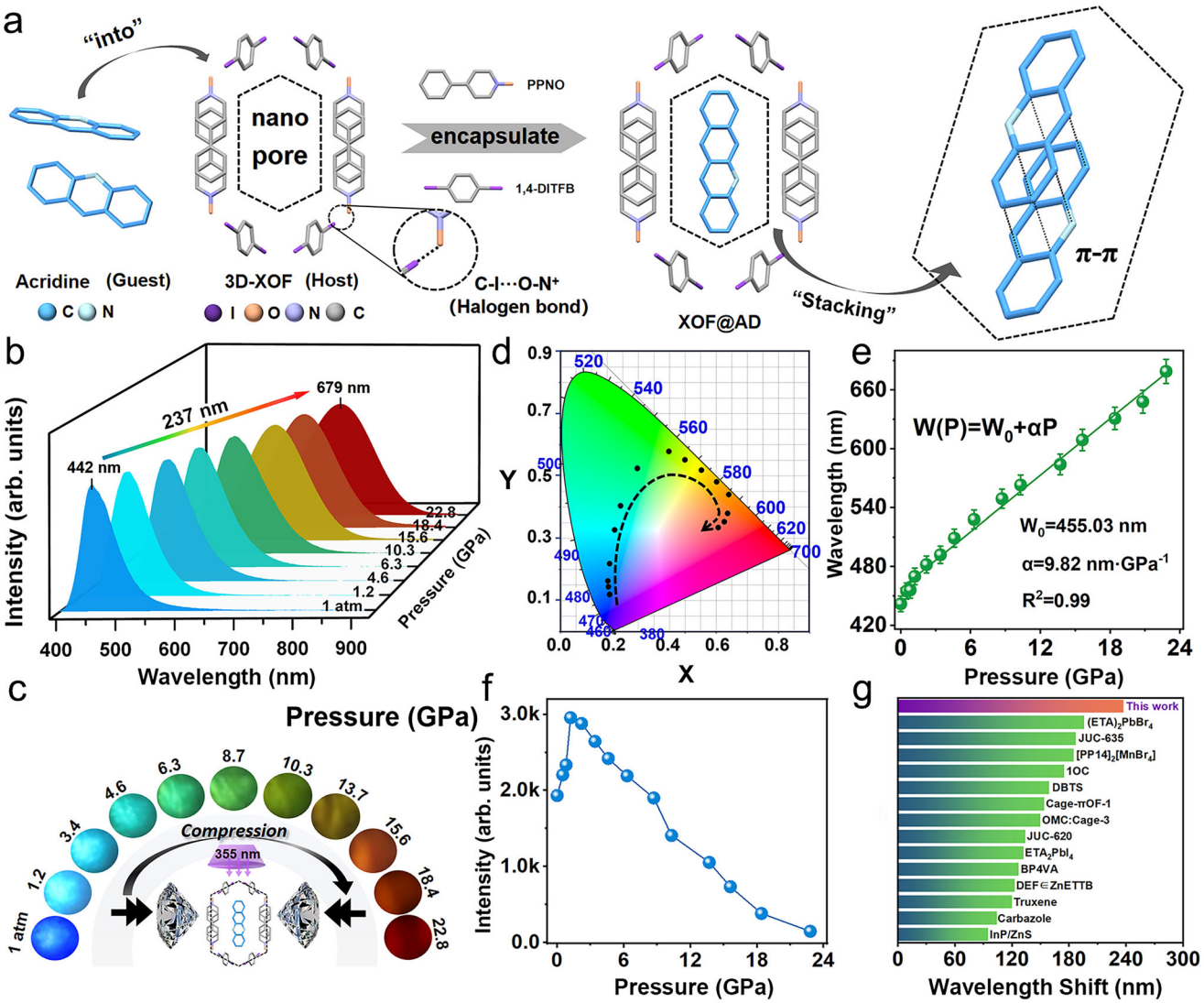

Fig. 2 | Crystal structure and PL behaviors of XOF@AD. a The crystal structure of XOF@AD at ambient conditions. The sky-blue and blue-white spheres represent C and N atoms of the guests, respectively. The purple, orange, blue-violet, and gray spheres represent I, O, N, and C atoms of the host, respectively. PPNO: 4-Phenylpyridine-N-oxide; 1,4-DITFB: 1,4-Diiodotetrafluorobenzene. 3D-XOF: three-dimensional halogen-bonded organic framework. **b** Normalized PL spectra of XOF@AD during compression. **c** Optical images of XOF@AD from 1 atm to 22.8 GPa. **d** The CIE chromaticity diagram of XOF@AD during compression. **e** Pressure-dependent PL wavelength evolution of XOF@AD during compression, with error bar denoting the standard deviation. **f** The PL intensity of XOF@AD as a function of pressure. **g** The piezochromic performance of materials was reported in the literature and this work within the visible range[8,13–15,32–41].

resolved photoluminescence (TRPL) measurements to systematically investigate the pressure-dependent PL decay kinetics (Supplementary Fig. 7). Analysis of the PL decay dynamics revealed that non-radiative decay rates (κ_{nr}) significantly exceeded radiative decay rates (κ_r) across during compression. This dominance of κ_{nr} over κ_r fundamentally governs the pressure-dependent evolution of PLQY. Crucially, the κ_{nr} values for XOF@AD remained suppressed under 1.2 GPa, which directly accounts for the enhanced PL emission intensity and improved PLQY[31]. Notably, XOF@AD exhibits a record-breaking piezochromic shift of 237 nm within the visible range, representing the largest chromatic modulation documented to date under hydrostatic compression (Supplementary Fig. 8 and Table 1). This performance outperforms all known pressure-responsive materials in visible chromatic range (Fig. 2g)[8,13–15,32–41].

Given that the PL of XOF@AD predominantly originates from the encapsulated AD guest molecules, we investigated the high-pressure PL behavior of AD (Supplementary Figs. 9, 10). At ambient conditions, AD exhibits bright blue emission centered at 462 nm with a 20 nm red-shift compared to XOF@AD. Analogous to XOF@AD, a PIEE phenomenon was also observed in AD up to 1.2 GPa. However, the PL emission of AD exhibits a lower pressure quenching threshold in contrasts to XOF@AD under continuous compression. A series of optical photomicrographs unambiguously capture the PL behavior of AD. The distinct PL behavior observed between XOF@AD and AD presumably originates from synergistic C–I···O–N$^+$ halogen bond and π–hole···π interactions within the 3D-XOF. These interactions stabilize rigid hexagonal-channels that spatially confine and protect AD guest molecules.

Evolution of crystal structure in XOF@AD under pressure

To elucidate the piezochromic behavior and pressure-dependent structure evolution of XOF@AD, in situ high-pressure angle-dispersive synchrotron X-ray diffraction (ADXRD) measurements were conducted from 1 atm to 22.8 GPa (Fig. 3a and Supplementary Fig. 11a). The ADXRD profiles reveal gradual shifts of Bragg reflections toward higher 2θ angles, consistent with uniform lattice contraction under

https://doi.org/10.1038/s41467-026-68381-9

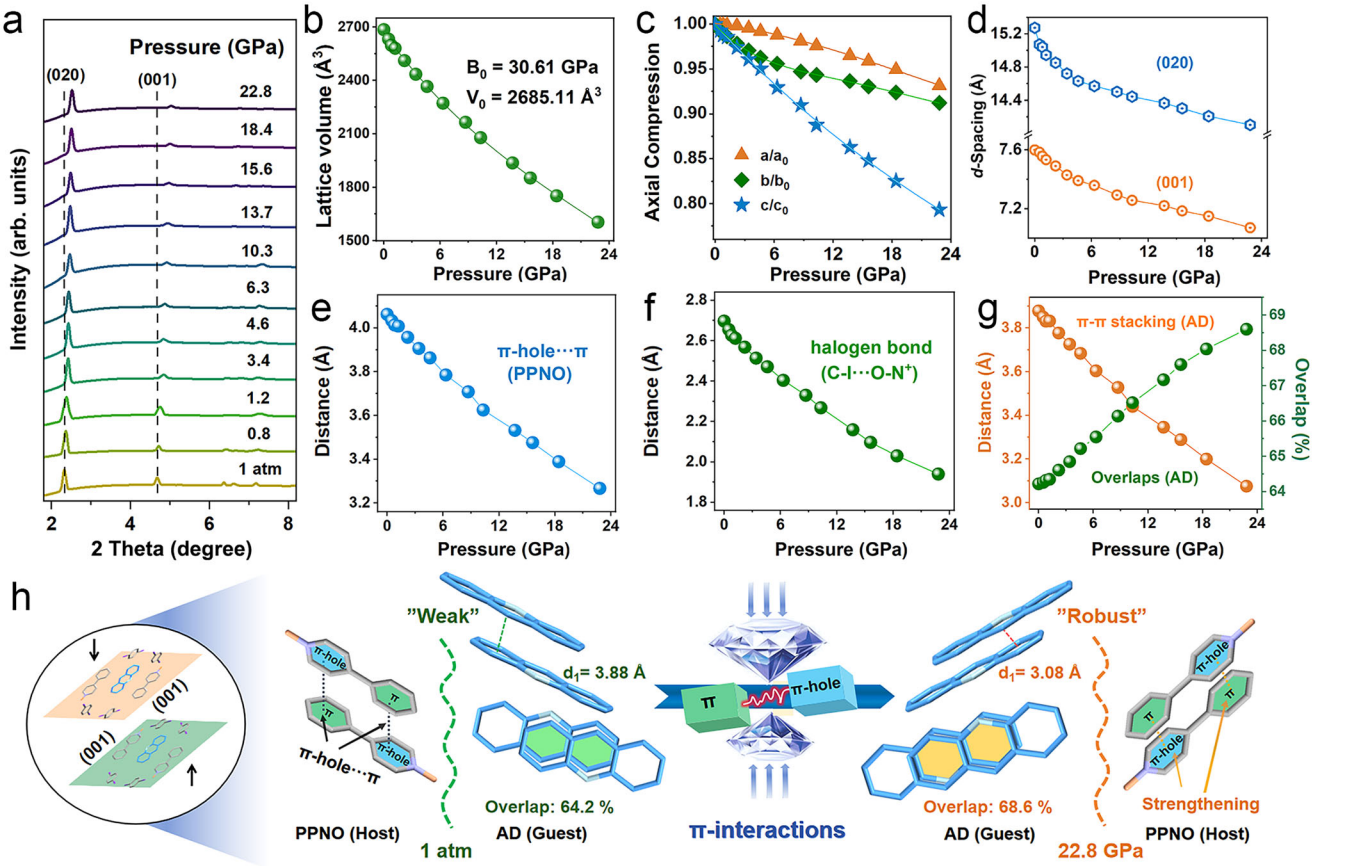

Fig. 3 | The evolution of crystal structure in XOF@AD under pressure. **a** Representative ADXRD patterns for XOF@AD as a function of pressure. **b** Cell volume evolution of XOF@AD upon pressure. **c** The compression rate of lattice constants of XOF@AD during compression. **d** Selected *d*-spacings of XOF@AD as a function of pressure. **e** The π−hole···π distance of 3D-XOF host during compression. **f** The halogen bond distance of 3D-XOF host during compression. **g** The π−π stacking distance and overlaps of AD guests during compression. **h** Evolution diagram of pressure-modulated π−interactions in XOF@AD. π−Interactions include π−π stacking interactions and π−hole···π interactions.

hydrostatic compression. Notably, no abrupt peak splitting or emergence of new reflections is observed throughout the compression cycle, indicating the absence of phase transitions. We used the General Structure Analysis System (GSAS) software to characterize the structural variations of XOF@AD via Rietveld refinement. At ambient conditions, the refinement of ADXRD pattern matches well with the experimental results (R_{wp} = 0.84%, R_p = 0.46%) through validation of the initial *C*2/*c* space group assignment.

We utilized the three-order Birch-Murnaghan equation of state to fit the pressure-volume data obtained in the experiment under high pressure[42,43]. The continuous volumetric contraction suggests no abrupt crystal or electronic structural phase transitions in XOF@AD from 1 atm to 22.8 GPa (Fig. 3b). Figure 3c illustrates the anisotropic compressibility of lattice parameters under pressure, where distinct axial compression rates reflect the structural anisotropy of XOF@AD. The *c*-axis exhibits the most compressibility compared to the *a*-axis and *b*-axis, evidenced by the progressive decrease in (001) plane *d*-spacings that reflects its greater pressure sensitivity (Fig. 3d). The continuous compression of the (001) planes led to progressive strengthening of π−π stacking interactions and π−hole···π interactions. Simultaneously, the enhancement of C−I···O−N^+ halogen bond correlates with the gradual contraction in the *d*-spacings of the (020) planes during compression. Under hydrostatic compression, the π−hole···π distance along the *c*-axis exhibited a significant reduction, synergistically cooperating with the progressively enhanced halogen bond to collectively maintain the structural rigidity of 3D-XOF (Fig. 3e, f). This structural evolution likely suppresses the amorphous transition of AD guests within 3D-XOF to enable the observation of the PL emission under high pressure. More notably, the π−π stacking distance between AD guests decreased nearly linearly, accompanied by a progressive increase in stacking overlaps, which is identified as the critical determinant enabling the realize of full-visible-spectrum piezochromism (Fig. 3g). To further assess the protective role of the 3D-XOF host on AD guests under high pressure, ADXRD measurements were conducted on AD under pressure conditions (Supplementary Fig. 11b). At ambient conditions, the Rietveld refinement of the ADXRD patterns agreed well with the experimental data (R_{wp} = 0.57%, R_p = 0.35%). In stark contrast to XOF@AD, AD exhibited severe pressure-induced amorphization, directly correlating with the PL quenching under high pressure. This pronounced structural contrast provides definitive evidence that the 3D-XOF effectively suppresses configurational disorder of the encapsulated AD guests during compression. Supported by enhanced π−hole···π interactions, the π−π stacking distance of AD guests decreases nearly linearly from 3.88 to 3.08 Å during compression (Fig. 3h)[44–46]. The π−π stacking overlaps ratio increases from 64.2% at ambient pressure to 68.6% at 22.8 GPa. These coordinated π−interactions directly correlate with the full-visible-spectrum piezochromic behavior observed in XOF@AD during compression[47].

High-pressure IR and Hirshfeld surface analysis of XOF@AD under pressure

To further validate the pressure-induced evolution of molecular interactions underlying the pronounced piezochromism, we carried out in situ high-pressure infrared (IR) spectroscopy on XOF@AD

https://doi.org/10.1038/s41467-026-68381-9

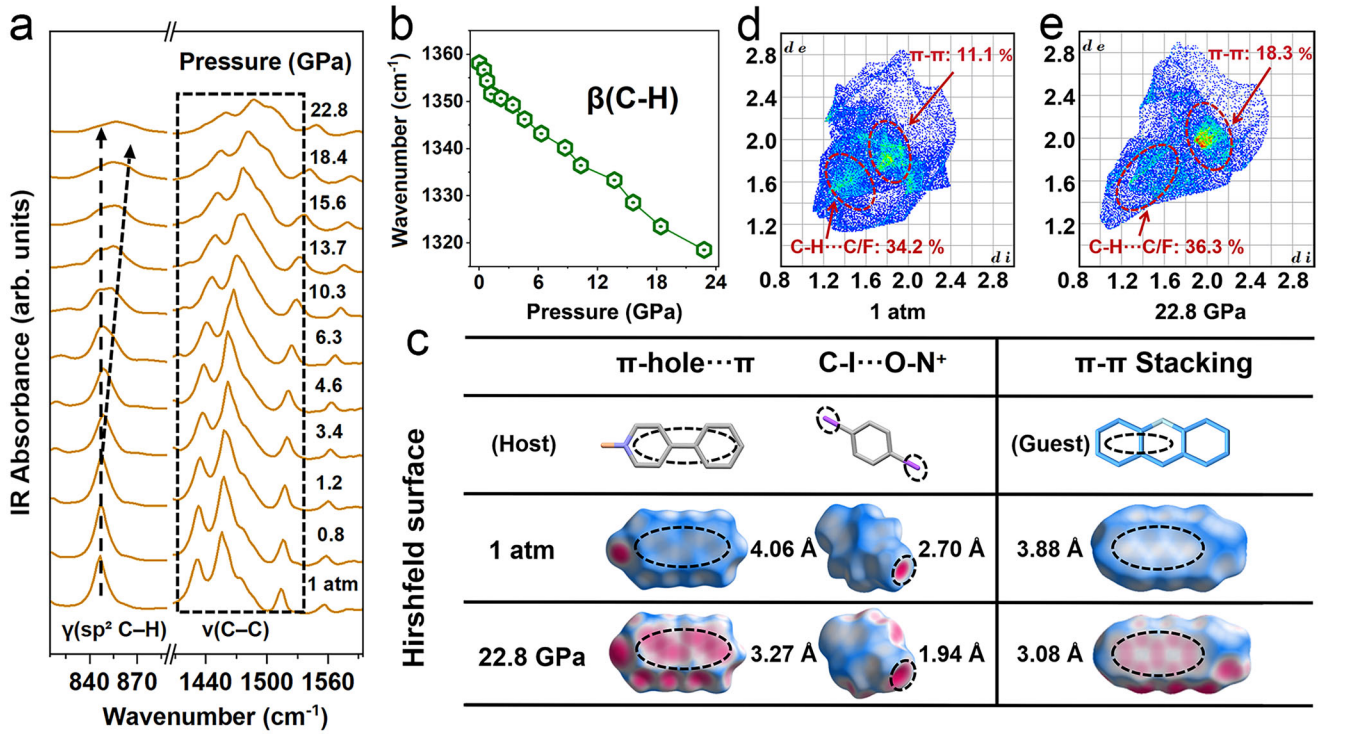

Fig. 4 | The evolution of intermolecular interactions in XOF@AD under pressure. a IR spectra of XOF@AD at selected pressures up to 22.8 GPa. **b** IR vibration modes of β (C–H) with respect to pressure. **c** Hirshfeld surface diagrams of XOF@AD at 1 atm and 22.8 GPa. **d** The finger-print plot of AD guests at 1 atm. **e** The finger-print plot of AD guests at 22.8 GPa.

(Fig. 4a and Supplementary Fig. 12). The vibrational bands at 850 cm^{-1} and 750 cm^{-1} are respectively assigned to the out-of-plane γ(sp^2 C–H) bending and φ(sp^2 C–C) ring deformation modes[39]. Both modes exhibit negligible frequency variation below 1.2 GPa, contrary to the conventional pressure-dependent blue-shift trend. This anomalous behavior implies significantly strengthened intermolecular interactions within XOF@AD. Such interactions rigidify molecular conformations and suppress non-radiative vibrational dissipation, thereby amplifying radiative recombination efficiency and driving the PIEE phenomenon. Moreover, the spectral region between 1400 and 1600 cm^{-1} corresponds to the ν(C–C) aromatic ring breathing modes. The typical broadening and splitting of ν(C–C) directly confirm the enhancement of π–π stacking interactions[48,49]. The absorption band at 1358 cm^{-1} is assigned to the in-plane β(C–H) bending mode of the benzene ring at ambient conditions (Fig. 4b)[50]. This continuous red-shift vibrational mode of ~40 cm^{-1} represents progressive strengthening of C–H···C hydrogen bond interaction during hydrostatic compression. The accelerated red-shift of the β(C–H) mode from 1 atm to 1.2 GPa potentially correlates with the PIEE phenomenon. Most IR vibrational modes show blue-shift accompanied by splitting and broadening under further compression, which indicates that π–π stacking interactions become more pronounced. This enhancement promotes substantial increases in non-radiative decay that leads to a gradual decline in PL emission until complete quenching occurs.

Based on the Rietveld refinements, we conducted complementary Hirshfeld surface calculations to systematically investigate non-covalent interactions in XOF@AD (Fig. 4c). Hirshfeld surfaces analysis at 22.8 GPa revealed intensified intermolecular interactions, manifested through expanding red regions that contrasted with ambient-pressure blue zones characteristic of weaker interactions. We established a quantitative model by using the aromatic fused ring of AD as the reference plane to calibrate critical intermolecular distances (Supplementary Fig. 13). d_1 corresponds to π–π stacking interactions of guests, d_2 and d_3 to C–H···C and C–H···F hydrogen bonds, while d_4 and d_5 represent π–hole···π interactions and halogen bonding, respectively. Consistent with the behavior of ν(C–C) in IR measurements, the progressive reduction of d_1 from 3.88 Å to 3.08 Å under pressure correlates with a marked enhancement of π–π stacking interactions, as evidenced by their increased contribution to finger-print plot from 11.1 to 18.3% (Fig. 4d, e). The systematic decrease in d_2 and d_3 distances drives the increase in hydrogen bond contribution from 34.2 to 36.3%, which correlates with the red-shift in-plane β(C–H) bending and enhances these non-covalent interactions. Notably, the weaker enhancement of chemical bond interaction compared to π–π stacking interactions establishes a competitive interplay between these mechanisms. The initial PIEE is rationalized by the restriction of chemical bond vibrations-mediated suppression of non-radiative decay, whereas the eventual PL quenching at elevated pressures is dominated by π–π stacking interactions. The pressure-dependent evolution of distances demonstrated progressive reductions in d_4 from 4.06 to 3.27 Å and in d_5 from 2.70 to 1.94 Å to strongly support the formation of a more rigid 3D-XOF. Concurrently, the relative contributions of π–hole···π interactions and halogen bond increased significantly from 24.8 to 30.1% and from 9.4 to 11.8%, respectively (Supplementary Figs. 14, 15). These molecular interactions evolution directly provide evidence for the pressure-induced suppression of guest amorphization within rigid 3D-XOF, which suggest the maintenance of the parallel-offset π–π stacking arrangement of guest molecules during compression.

Full-visible-spectrum piezochromism and PIEE mechanism of XOF@AD

To directly elucidate the mechanism underlying the full-visible-spectrum piezochromism phenomenon, in situ pressure-dependent absorption spectroscopy was conducted on XOF@AD (Fig. 5a and Supplementary Fig. 16). At ambient conditions, XOF@AD exhibited an absorption edge at 426 nm and appeared nearly colorless. Under progressive compression, the absorption edge undergoes continuous

https://doi.org/10.1038/s41467-026-68381-9

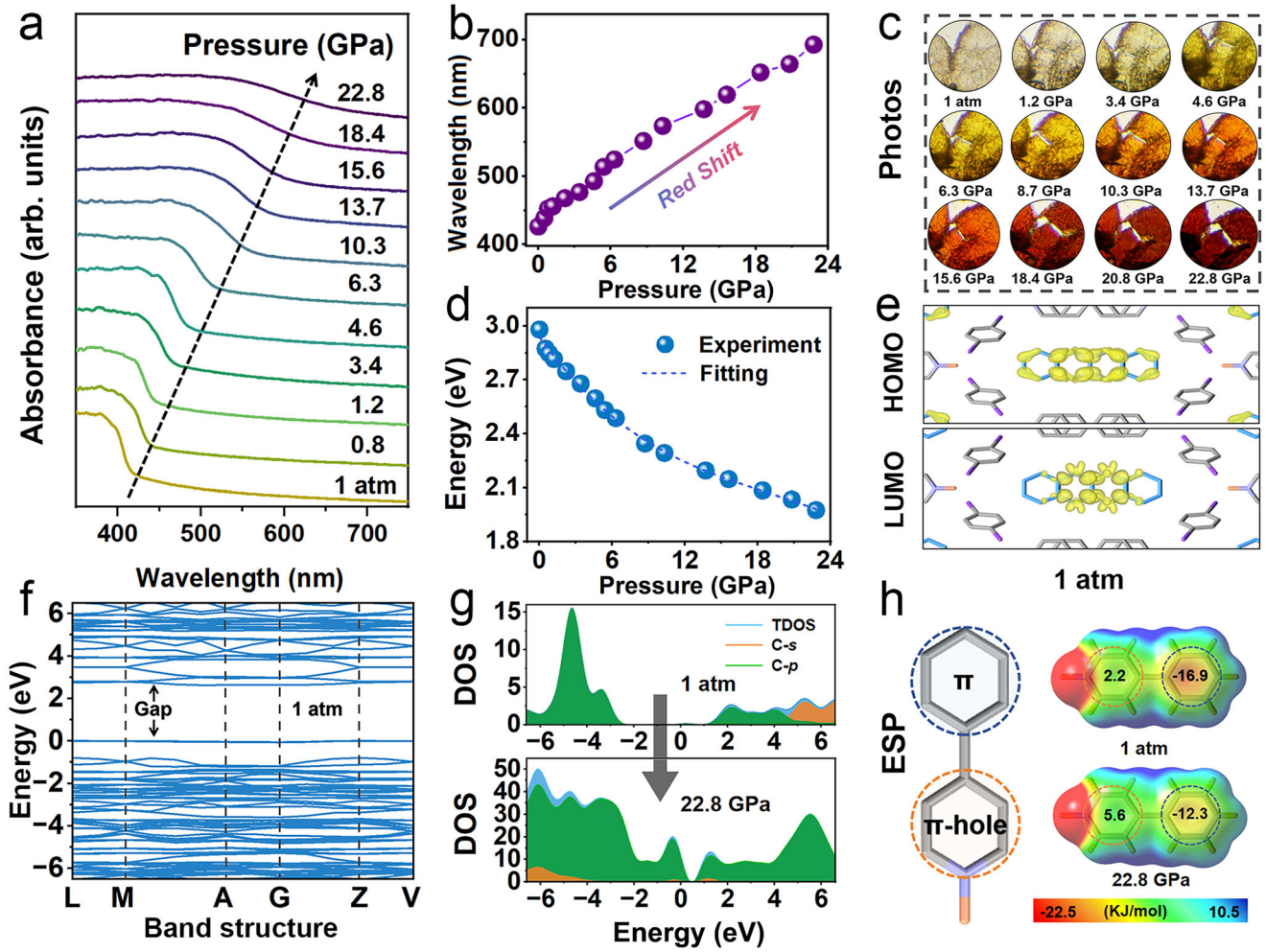

Fig. 5 | Full-visible-spectrum piezochromism mechanism of XOF@AD. a High pressure UV-vis absorption spectra of XOF@AD. **b** The wavelength of absorption edge during compression. **c** Color evolution of XOF@AD during compression. **d** Band gap changes of XOF@AD as a function of pressure. **e** Orbital profiles of HOMO and LUMO of XOF@AD at ambient conditions. **f** Band structure of XOF@AD at ambient conditions. **g** Total and projected density of states (DOSs) of isolated atoms for C at 1 atm and 22.8 GPa. **h** ESP analyses of PPNO at 1 atm and 22.8 GPa.

red-shift to ~693 nm, accompanied by a chromatic transition from nearly colorless through orange to deep red (Fig. 5b, c). This spectral evolution displays a systematic strengthening of intermolecular interactions coupled with reduced intermolecular distances. By constructing Tauc plots of $(\alpha h\nu)^2$ versus $h\nu$ plots under high pressure, the progressive narrowing of band gap from 2.98 eV to 1.98 eV was revealed (Supplementary Fig. 17). This directly demonstrates that the pressure-dependent electronic structure modulation is dominated by the enhanced π−π stacking interactions (Fig. 5d)[51,52]. For comparison, we also carried out in situ pressure-dependent absorption spectroscopy on AD (Supplementary Fig. 18). The absorption edge of AD displays a gradual red-shift up to 15.6 GPa during compression, and the band gap derived from the Tauc plot analysis exhibits a steady decrease from 2.75 to 1.76 eV (Supplementary Fig. 19). Nevertheless, a clear turning point emerges beyond 15.6 GPa, followed by an increase to 1.83 eV at 22.8 GPa. This indicates that an electronic structural transformation has occurred, which can also be correlated with the increased degree of structural disorder under pressure. These results provide compelling evidence that the rigid 3D-XOF host effectively maintains the π−π stacking configuration of AD guests, thereby confirming that the enhanced π−π stacking interactions under high pressure are the origin of the observed full-visible-spectrum piezochromic behavior. In addition, we carried out geometry optimization and calculated the band gap with the density of states (DOS) in XOF@AD based on density functional theory (DFT)[53]. At ambient conditions, both the highest occupied molecular orbital (HOMO) and the lowest unoccupied molecular orbital (LUMO) are localized exclusively on guests, indicating that PL emission originates predominantly from AD (Fig. 5e). This initial deep-blue PL emission arises from the ππ* electronic transition within AD, which is a critical prerequisite for achieving full-visible-spectrum piezochromism under high pressure. To further elucidate the mechanism of PIEE, we performed time-dependent DFT (TDDFT) calculations at the M06-2X/Def2-TZVP level for pressures below 1.2 GPa to investigate the excited-state electronic transitions in XOF@AD (Supplementary Fig. 20). The oscillator strength increased from 0.1105 at 1 atm to 0.1339 at 1.2 GPa, reflecting the strengthened transition dipole moment under high pressure (Supplementary Fig. 21). This provides further evidence for the continuous increase of the κ_r (Supplementary Fig. 7). Therefore, the restriction of chemical bond vibrations significantly suppresses non-radiative decay, which effectively accounts for the PIEE phenomenon in XOF@AD. Figure 5f and Supplementary Fig. 22 illustrate the pressure-dependent evolution of simulated band gap under progressive compression. The calculated band gap narrowing trend aligns with experimental absorption data confirms the consistency between theoretical and experimental results, and the enhancement in the DOS dominated by C-*p* orbital contributions further corroborates the band gap narrowing (Fig. 5g). These synergistic electronic effects of

intensified DOS contributions and reduced band gap collectively underscore the pivotal role of pressure-induced π−π stacking interactions enhancement in governing electronic modulation[54]. To investigate the pressure-induced suppression of guest amorphization within 3D-XOF, we analyzed calculations of electrostatic surface potentials (ESP) for PPNO through preferential *c*-axis compression at the level of M06-2X/6-311G(d) (Fig. 5h). The elevated ESP values correlated with strengthened π−hole···π interactions drive tighter PPNO stacking that amplifies non-covalent intermolecular forces, thereby lowering the interaction energy of the 3D-XOF host to enhance stability[55–57]. Further quantitative analysis of the π−hole···π interaction energy showed a decrease from −3.00 kcal·mol^{-1} at 1 atm to −3.23 kcal·mol^{-1} at 22.8 GPa, directly demonstrating that this strengthening interaction effectively stabilizes the structure (Supplementary Fig. 23)[58,59]. This preserves the parallel-offset π−π stacking alignment of AD guests and prevents their disordering by maintaining the rigidity of the 3D-XOF structure. This stabilization mechanism critically accounts for the observation of piezochromic behavior under high pressure. Both experiments and calculations conclusively validate that the host-guest strategy effectively maintains the structural rigidity, which enables manipulating full-visible-spectrum piezochromism through pressure-modulated π−interactions.

Discussion

In summary, we have harnessed the host-guest strategy to preserve structural rigidity and successfully manipulated full-visible-spectrum piezochromism in XOF@AD accompanied by a remarkable 237 nm red-shift. The PL emission is tunable from deep blue (2.81 eV) to red (1.83 eV), which spans nearly the entire visible spectrum and demonstrates the highest performance reported to date. The PL wavelength exhibits near-linear variation with maintained piezochromic performance over two pressurization cycles to establish XOF@AD as a reliable pressure calibration standard under extreme pressure conditions. In light of both experimental and calculation results, the reinforced π−hole···π interactions contribute to the structural rigidity of the 3D-XOF by lowering the interaction energy. Such rigidity effectively inhibits the amorphous transition of AD guests and enhances their π−π stacking configuration, which accounts for the full-visible-spectrum piezochromism. Meanwhile, the PIEE behavior under the pressure of 1.2 GPa was observed that arises from inhibited non-radiative decay pathways through the restriction of chemical bond vibrations. These findings establish a promising design strategy for piezochromic materials through the host-guest strategy, enabling significant applicability in optical pressure-responsive detection and broadening the horizons of intelligent luminescence materials.

Methods

Materials

All chemicals were purchased from Shanghai Titan Scientific Co., Ltd and used directly without further purification. 1,4 diiodotetrafluorobenzene (1,4-DITFB, Adamas-beta, 99%), 4-Phenylpyridine-N-oxide (PPNO, Adamas-beta, 98%), Acridine (AD, Adamas-beta, 98%), Acetone (GENERAL-REAGENT, 99.5%), Ethanol (GENERAL-REAGENT, 99.7%).

Growth of XOF@AD and 3D-XOF Cocrystals

XOF@AD were synthesized referring to the "HAD" in the literature method by cocrystal engineering with further improvements. 1,4-DITFB (40.2 mg, 0.1 mmol), PPNO (17.1 mg, 0.1 mmol) and AD (17.9 mg, 0.1 mmol) were absolutely dissolved in 10 mL acetone with a molar ratio of 1:1:1 in a glass culture dish, then sealed the culture dish with Parafilm and quickly poked some small holes with the needle. The acetone would evaporate completely within 5 days. The light yellow cocrystals at the bottom were collected. Ethanol was used to remove unreacted impurities from the cocrystals surface to obtain XOF@AD cocrystals (yield: ~64%). A bright deep blue emission can be seen under 365 nm UV light. The samples were directly stored in sample vials under ambient conditions without requiring any special storage precautions.

The 3D-XOF was synthesized following a procedure analogous to that described above. Specifically, 1,4-DITFB (40.2 mg, 0.1 mmol) and PPNO (17.1 mg, 0.1 mmol) were completely dissolved in 8 mL of acetone at a 1:1 molar ratio in a glass culture dish. The dish was then sealed with Parafilm, and several small holes were carefully punctured in the sealing film using a needle. The acetone was allowed to evaporate completely over a period of 3 days. Subsequently, the resulting cocrystals were washed with ethanol to remove any unreacted impurities, yielding the final 3D-XOF cocrystals (yield: ~57%).

In situ high pressure experiments

In all experiments, we used the same symmetric DAC which has a pair of type IIa ultra-low fluorescence diamonds with a diameter of 400 μm to generate high pressure at room temperature. We loaded the sample into a T301 steel gasket featuring a 150 μm diameter cavity and a 45 μm pre-indentation thickness. The co-crystallized XOF@AD single crystals of millimeter scale were ground to fit the 150 μm sample chamber for all in situ high-pressure experiments. The pressure in DAC was calibrated using the ruby fluorescence technology. Silicon oil (Aldrich) was used as the pressure transmitting medium for PL, UV-visible absorption, angle-dispersive X-ray diffraction (ADXRD) and TRPL measurements; whereas KBr (Adamas-beta, 99.9%) was employed for the FT-IR measurements.

The in situ high-pressure PL spectra measurements of XOF@AD were recorded by an optical fiber spectrometer (Ocean Optics, QE65000) with the data-collection time of 2000 ms. A 355 nm line of a UV DPSS laser with the power of 10 mW was used for PL measurements. PL images of XOF@AD were obtained using a camera (Canon EOS 5D Mark II) equipped on a microscope (Ecilipse TI-U, Nikon). The complete procedure, including compression, calibration, and spectral collection, required ~30 s, with no deliberate pressure-holding step incorporated into the measurement cycle.

The in situ high-pressure UV-visible absorption measurements of XOF@AD were similarly recorded by an optical fiber spectrometer (Ocean Optics, QE65000) with the data-collection time of 300 ms. A deuterium-halogen light was used for the UV-visible absorption measurements. The corresponding images of XOF@AD were obtained using a camera (Canon Eos 5D mark II).

The in situ high-pressure FT-IR absorption measurements of XOF@AD were carried out by using a Bruker Vertex 70 V FT-IR spectrometer (BRUKER OPTIK GMBH, Germany) equipped with a nitrogen-cooled mercury-cadmium-telluride detector.

The in situ high-pressure TRPL measurements of XOF@AD which are performed to investigate the PL decay kinetics were measured using a 405 nm pulsed diode laser as excitation source with the focal length grating spectrograph (HRS-300 MS, PI).

In situ X-ray diffraction (XRD) measurements

The powder XRD (P-XRD) data at ambient condition was measured by using Cu as the target, then the experimental data was obtained from 4 to 50 degrees (R-AXIS RAPID II, Rigaku). The corresponding in situ high-pressure ADXRD experiments were carried out at Shanghai Synchrotron Radiation Facility (SSRF), beamline 15U1 (BL15U1). X-ray beam with a diameter of about 5 μm and wavelengths of 0.6199 Å was used in the diffraction experiment. CeO_2 was employed for the standard sample to calibrate. The image obtained by experiment were comprehensively analyzed using the Dioptas program, exporting as the 1-dimensional intensity versus 2-theta diffraction angle pattern.

Method of calculations

Based on the Rietveld refinements, we obtained the high-pressure structures of XOF@AD during compression. We got the

symmetrical crystal structure model by occupying half an atom of N in AD. By using the Crystal Explorer 17.5 program, we analyzed and visualized the interactions in XOF@AD. The corresponding 3D Hirshfeld surfaces and finger-print maps during compression were obtained.

The first-principles calculations of geometry optimizations and band gaps were carried out by using the Cambridge Sequential Total Energy Package (CASTEP), with the Perdew-Burke-Ernzerhof (PBE) exchange-correlation functional within the generalized gradient approximation framework of DFT. Grimme's approach and the DFT-D3 correction method were employed to describe long-range van der Waals interactions.

The Charge density difference diagrams and interaction energy were described by using the Vienna Ab initio Simulation Package with the PBE as the exchange-correlation function and the frozen-core projector-augmented wave pseudopotentials as parameterization with a plane-wave cutoff energy of 500 eV. The long-range van der Waals interactions were also accounted for using Grimme's DFT-D3 method with Becke-Johnson damping.

The calculations of excited state electronic transitions of XOF@AD were performed using Gaussian09 program by TDDFT method at the M06-2X/Def2-TZVP level. The maps (electron density 0.001 e·Bohr^{-3}) of ESP of PPNO were calculated under the level of M06-2X/6-311G(d), the color range maps from red to blue corresponds to ESP from negative to positive.

Data availability

All data are available from the corresponding author upon request. Source data are provided with this paper.

Code availability

Gaussian 09 code is available for download on the developer page: https://gaussian.com/.

References

1. Ge, Y. et al. A distinctive HPHT platform with different types of large-volume press subsystems at SECUF. *Matter Radiat. Extrem.* **9**, 063801 (2024).
2. Xu, T. et al. Room-temperature phosphorescence and anomalous piezochromism in molecular crystals enabled by iodine atomic orbital sharing. *Nat. Commun.* **16**, 3550 (2025).
3. Guo, S., Zhan, Y. & Lü, X. High-pressure research on optoelectronic materials: insights from in situ characterization methods. *Matter Radiat. Extrem.* **10**, 033802 (2025).
4. Chu, B. et al. Enabling nonconjugated polyesters emit full-spectrum fluorescence from blue to near-infrared. *Nat. Commun.* **15**, 366 (2024).
5. Wu, J. et al. Phase engineering for achieving full-color tunable emission from blue to red and multi-level information security in isomeric hybrid copper halides. *Angew. Chem. Int. Ed.* **64**, e202506748 (2025).
6. Yang, J. et al. Phase stability and electronic structure of $CsPbBr_3$ perovskites under rare-earth doping and hydrostatic pressure. *J. Mater. Sci.* **59**, 4586–4595 (2024).
7. Xie, H. et al. Tethered helical ladder-type aromatic lactams. *J. Am. Chem. Soc.* **146**, 11978–11990 (2024).
8. Dong, Y. et al. Multi-stimuli responsive fluorescence switching: the reversible piezochromism and protonation effect of a divinylanthracene derivative. *J. Mater. Chem. C.* **1**, 7554–7559 (2013).
9. Guo, T., Hu, P., Li, L., Wang, Z. & Guo, L. Amorphous materials emerging as prospective electrodes for electrochemical energy storage and conversion. *Chem* **9**, 1080–1093 (2023).
10. Li, X. et al. Tuneable near white-emissive two-dimensional covalent organic frameworks. *Nat. Commun.* **9**, 2335 (2018).
11. Haug, W. K., Moscarello, E. M., Wolfson, E. R. & McGrier, P. L. The luminescent and photophysical properties of covalent organic frameworks. *Chem. Soc. Rev.* **49**, 839–864 (2020).
12. Zhao, Z. et al. Non-aromatic annulene-based aggregation-induced emission system via aromaticity reversal process. *Nat. Commun.* **10**, 2952 (2019).
13. Fang, J. et al. Piezofluorochromism in covalent organic frameworks: pressure-induced emission enhancement and blue-shifted emission. *Angew. Chem. Int. Ed.* **63**, e202409099 (2024).
14. Cui, D. et al. Piezofluorochromism in hierarchical porous π-stacked supermolecular spring srameworks from aromatic chiral cages. *Angew. Chem. Int. Ed.* **63**, e202319815 (2024).
15. Zhu, Z. H. et al. Smart tetraphenylethene-based luminescent metal–organic frameworks with amide-assisted thermo-fluorochromics and piezofluorochromics. *Adv. Sci.* **9**, 2200850 (2022).
16. Sun, D. et al. The host–guest inclusion driven by host-stabilized charge transfer for construction of sequentially red-shifted mechanochromic system. *Nat. Commun.* **14**, 4190 (2023).
17. Fan, C., Wu, W., Chruma, J. J., Zhao, J. & Yang, C. Enhanced triplet–triplet energy transfer and upconversion fluorescence through host–guest complexation. *J. Am. Chem. Soc.* **138**, 15405–15412 (2016).
18. Xue, N. et al. A general supramolecular strategy for fabricating full-color-tunable thermally activated delayed fluorescence materials. *Nat. Commun.* **15**, 1425 (2024).
19. Bai, X. et al. Halogen-bonded organic frameworks (XOFs) based on N···Br^+···N bonds: robust organic networks constructed by fragile bonds. *Angew. Chem. Int. Ed.* **63**, e202408428 (2024).
20. Gong, G. et al. Halogen-bonded organic framework (XOF) based on iodonium-bridged N···I^+···N interactions: a type of diphase periodic organic network. *Angew. Chem. Int. Ed.* **60**, 14831–14835 (2021).
21. Ding, X.-H. et al. Halogen bonding in the co-crystallization of potentially ditopic diiodotetrafluorobenzene: a powerful tool for constructing multicomponent supramolecular assemblies. *Natl. Sci. Rev.* **7**, 1906–1932 (2020).
22. Liu, R., Gao, Y. J. & Jin, W. J. Color-tunable phosphorescence of 1,10-Phenanthrolines by 4,7-methyl/-diphenyl/-dichloro substituents in cocrystals assembled via bifurcated C—I···N halogen bonds using 1,4-diiodotetrafluorobenzene as a bonding donor. *Acta Crystallogr. Sect. B* **73**, 247–254 (2017).
23. Wang, H. & Jin, W. J. Cocrystal assembled by 1,4-diiodotetra-fluorobenzene and phenothiazine based on C—I···π/N/S halogen bond and other assisting interactions. *Acta Crystallogr. Sect. B* **73**, 210 (2017).
24. Li, L., Wang, H., Wang, W. & Jin, W. J. Interactions between halo-perfluorobenzenes and fluoranthene in luminescent cocrystals from π-hole···π to σ-hole···π bonds. *CrystEngComm* **19**, 5058–5067 (2017).
25. Wu, W. X., Wang, H. & Jin, W. J. Various guest PAHs locked into a soft-cavity-type host assembled via halogen bonds to form luminescent cocrystals. *CrystEngComm* **22**, 5649–5655 (2020).
26. Yang, J., Fang, M. & Li, Z. Organic luminescent materials: the concentration on aggregates from aggregation-induced emission. *Aggregate* **1**, 6–18 (2020).
27. Luo, H. et al. Pressure aging: an effective process to liberate the power of high-pressure materials research. *Proc. Natl. Acad. Sci.* **121**, e2416835121 (2024).
28. Wu, W. X., Wang, H. & Jin, W. J. Pure organic hexagonal–channels constructed by C–I···–O–N^+ halogen bond and π–hole···π bond under mediation of guest. *Cryst. Growth Des.* **18**, 6742–6747 (2018).
29. Wang, Y. et al. Reaching 90% photoluminescence quantum yield in one-dimensional metal halide $C_4N_2H_{14}PbBr_4$ by pressure-suppressed nonradiative loss. *J. Am. Chem. Soc.* **142**, 16001–16006 (2020).

30. Ai, L. et al. Tailored fabrication of full-color ultrastable room-temperature phosphorescence carbon dots composites with unexpected thermally activated delayed fluorescence. *Adv. Mater.* **36**, 2401220 (2024).
31. Zhang, Y., Liu, H. & Weng, Y. Theoretical and experimental investigation of the electronic propensity rule: a linear relationship between radiative and nonradiative decay rates of molecules. *J. Phys. Chem. Lett.* **14**, 4151–4157 (2023).
32. An, L. C. et al. Near-full-spectrum emission realized in a single lead halide perovskite across the visible-light region. *Angew. Chem. Int. Ed.* **63**, e202411298 (2024).
33. Fang, J. et al. Piezochromism in dynamic three-dimensional covalent organic frameworks. *Angew. Chem. Int. Ed.* **62**, e202304234 (2023).
34. Zhao, X. et al. Pressure-treated engineering to harvest enhanced green emission in Mn-based organic–inorganic metal halides at ambient conditions. *Adv. Funct. Mater.* **32**, 2109277 (2022).
35. Wang, L. et al. Luminescent chromism of boron diketonate crystals: distinct responses to different stresses. *Adv. Mater.* **27**, 2918–2922 (2015).
36. Fu, Z. et al. Pressure-induced emission enhancement by restricting chemical bond vibration. *J. Mater. Chem. C.* **9**, 14578–14582 (2021).
37. Li, Y. et al. Reticular modulation of piezofluorochromic behaviors in organic molecular cages by replacing non-luminous components. *Angew. Chem. Int. Ed.* **63**, e202403646 (2024).
38. Fang, Y. et al. Manipulating emission enhancement and piezochromism in two-dimensional organic-inorganic halide perovskite $[(HO)(CH_2)_2NH_3)]_2PbI_4$ by high pressure. *CCS Chem.* **3**, 2203–2210 (2021).
39. Wu, M. et al. Pressure-induced restricting intermolecular vibration of a herringbone dimer for significantly enhanced multicolor emission in rotor-free truxene crystals. *J. Phys. Chem. Lett.* **13**, 2493–2499 (2022).
40. Gu, Y. et al. Pressure-induced emission enhancement of carbazole: the restriction of intramolecular vibration. *J. Phys. Chem. Lett.* **8**, 4191–4196 (2017).
41. Liu, H. et al. Piezochromic luminescence in all-inorganic core–shell InP/ZnS nanocrystals via pressure-modulated strain engineering. *Nanoscale Horiz.* **5**, 1233–1239 (2020).
42. Guo, S. et al. Exciton engineering of 2D Ruddlesden–Popper perovskites by synergistically tuning the intra and interlayer structures. *Nat. Commun.* **15**, 3001 (2024).
43. Bu, K. et al. Nested order-disorder framework containing a crystalline matrix with self-filled amorphous-like innards. *Nat. Commun.* **13**, 4650 (2022).
44. Liu, Y. et al. Symmetry-engineered ultralong phosphorescence in double π-helical nanographenes. *Angew. Chem. Int. Ed.* **64**, e202515124 (2025).
45. Shao, B. et al. Luminescent switching and structural transition through multiple external stimuli based on organic molecular polymorphs. *J. Mater. Chem. C.* **7**, 3263–3268 (2019).
46. Li, G., Chu, Q., Yao, H., Wu, K. & She, Y.-B. High-performance deep-blue phosphorescent organic light-emitting diodes enabled by a platinum(ii) emitter. *Nat. Photon.* **19**, 977–984 (2025).
47. Guo, L. et al. Synergetic multiple charge-transfer excited states for anti-quenching and rapid spin-flip multi-resonance thermally activated delayed fluorescence emitter. *Adv. Mater.* **37**, 2500269 (2025).
48. Wang, Y. et al. Boosting multicolor emission enhancement in two-dimensional covalent–organic frameworks via the pressure-tuned π–π stacking mode. *Nano Lett.* **25**, 2141–2149 (2025).
49. Wu, W. X., Liu, M., Wang, H. & Jin, W. A simple rotor guest molecule mediates the formation of cage or channel structures of halogen-bonding host cocrystals. *Cryst. Growth Des.* **19**, 4378–4384 (2019).
50. Cole, K. C., Guevremont, J., Ajji, A. & Dumoulin, M. M. Characterization of surface orientation in poly(ethylene terephthalate) by front-surface reflection infrared spectroscopy. *Appl. Spectrosc.* **48**, 1513–1521 (1994).
51. Zhu, P. et al. Symmetry-driven engineering of long-range-ordered π–π stacking molecules for high-efficiency perovskite photovoltaics. *Nat. Synth.* https://doi.org/10.1038/s44160-025-00896-3 (2025).
52. Liu, Z., Lu, T. & Chen, Q. Intermolecular interaction characteristics of the all-carboatomic ring, cyclo[18]carbon: focusing on molecular adsorption and stacking. *Carbon* **171**, 514–523 (2021).
53. Lejaeghere, K. et al. Reproducibility in density functional theory calculations of solids. *Science* **351**, aad3000 (2016).
54. Cai, W. et al. Force-induced transition of π–π stacking in a single polystyrene chain. *J. Am. Chem. Soc.* **141**, 9500–9503 (2019).
55. Wu, Y. et al. Electrostatic potential as solvent descriptor to enable rational electrolyte design for lithium batteries. *Adv. Energy Mater.* **13**, 2300259 (2023).
56. Scheiner, S. Anatomy of π-hole bonds: linear systems. *J. Chem. Phys.* **155**, 174302 (2021).
57. Ju, H. et al. Tracking noncovalent interactions of π, π-hole, and ion in molecular complexes at the single-molecule level. *J. Am. Chem. Soc.* **146**, 25290–25298 (2024).
58. Chen, T. & Yan, D. Full-color, time-valve controllable and Janus-type long-persistent luminescence from all-inorganic halide perovskites. *Nat. Commun.* **15**, 5281 (2024).
59. Wang, L. et al. Multilayer assemblies of poly(4-vinylpyridine) bearing an osmium complex and poly(acrylic acid) via hydrogen bonding. *Macromol. Chem. Phys.* **200**, 1523–1527 (1999).

Acknowledgements

This work is supported by the National Natural Science Foundation of China (Nos. 12274177 to X.Y., 12304261 to Y.W. and T2521005 to B.Z.), the National Key R&D Program of China (Grant No. 2023YFA1406200 to X.Y.) and Jilin Provincial Health Research Talent Special Project (No. 2023SCZ83 to T.Z.). The Kawai-Type Large-Volume Press experiments and the spectral experiments were performed at the B1 and B2 stations, Synergetic Extreme Condition User Facility (SECUF). This work was mainly performed at BL15U1 at the Shanghai Synchrotron Radiation Facility (SSRF). The authors thank the staff from SSRF at BL15U1, and User Experiment Assist System.

Author contributions

X.Y. and B.Z. designed the project and supervised the work. B.Y., Y.W., J.L., K.Y., R.Q. and T.Z. performed the experiments, calculations and analyzed data. B.Y., Y.W., X.Y. and B.Z. wrote the manuscript.

Competing interests

The authors declare no competing interests.

Additional information

Supplementary information The online version contains supplementary material available at https://doi.org/10.1038/s41467-026-68381-9.

Correspondence and requests for materials should be addressed to Yixuan Wang, Tao Zhang, Xinyi Yang or Bo Zou.

Peer review information *Nature Communications* thanks Shigui Chen, Xujie Lü and the other, anonymous, reviewer(s) for their contribution to the peer review of this work. A peer review file is available.